Recovering Lithium Cobalt Oxide, Aluminium, and Copper from Spent Lithium-ion Battery via Attrition Scrubbing

Samuel D Widijatmoko, Gu Fu, Zheng Wang, Philip Hall

University of Nottingham
UK | CHINA | MALAYSIA

Faculty of Science and Engineering, University of Nottingham Ningbo China, 199 Taikang East Road, Ningbo, 315100, Zhejiang, China.

First published 2020

University of Nottingham
UK | CHINA | MALAYSIA

Recovering Lithium Cobalt Oxide, Aluminium, and Copper from Spent Lithium-ion Battery via Attrition Scrubbing

Samuel D Widijatmoko[a], Gu Fu[b,c], Zheng Wang[a], Philip Hall[a,d,*]

[a]Department of Chemical and Environmental Engineering, University of Nottingham Ningbo China, 199 Taikang East Road Ningbo 315100, China

[b]Department of Industrial Engineering, Zhejiang University, Hangzhou 310027, China

[c]National Institute of Innovation Management, Zhejiang University, Hangzhou 310027, China

[d] Ningbo New Materials Institute, The University of Nottingham, Ningbo, 315042, China

[*]Corresponding Author, Room 437 Peter Mansfield Building, 199 Taikang East Road Ningbo 315100, China

[*]E-mail: Philip.Hall@nottingham.edu.cn

Highlights

- Attrition scrubbing is effective in selectively concentrating $LiCoO_2$.
- Attrition scrubbing improves liberation efficiency from 34% to 77%.
- Attrition produces a precursor for hydrometallurgical processes.
- Electrostatic separator is used to recover copper and aluminium.

Abstract

In this manuscript, the results show that the single-stage liberation by using a cutting mill is sub-optimum. From the analysis, that the size fraction of < 850 μm only recovers 43.7 wt% LiCoO2. With the recovery of 9.0 wt% aluminium and 10.6 wt% copper the remainder of the copper being in the > 850 μm size fraction. The low recovery of LiCoO2 is caused by the particles that are still adhering on to the surface of the aluminium current collector. This lack of liberation prompted the use of attrition scrubbing as a secondary stage of mechanical treatment. 2.5 min Attrition scrubbing improves the selective liberation of cobalt towards aluminium and copper by 36.6 % and 42.6 % respectively. Attrition induces abrasion and it is shown to liberate the LiCoO2 particles. Results show a minimum of 80 wt% LiCoO2 particles can be recovered in the size fraction of < 38 μm with 7.0 wt% aluminium

and 6.1 wt% copper recovery, making attrition scrubbing a suitable second stage mechanical treatment for the recovery of LiCoO2.

Keywords: attrition scrubbing; liberation; lithium-ion battery; mechanical treatment; recycling

1 Introduction

Lithium-ion battery (LIB) technology has become the dominant energy storage for many consumer electronics and electric grids (Blomgren, 2017; Dunn et al., 2011). Despite the advancement of battery technology, present LIBs meet most of the requirements dictated by the large volume of the application linked to renewable energy and electric transportation field (Winslow et al., 2018). The spent LIBs from electric vehicles will emerge as the future waste problem with at least 25 billion units and 500 thousand tonnes of spent LIBs would be generated by 2020 (Richa et al., 2014; Zeng et al., 2014). When considering the natural scarcity and the demand projected for materials used in LIB production, cobalt is the most critical material as the demand for the future types of LIB is likely to contain embedded cobalt (Zubi et al., 2018).

In recent years, much research has been focused on developing efficient recovery methods for the materials found in spent LIBs. With the positive electrode active materials as the main targeted component as it is where the incentive of LIBs recycling come from (Gaines, 2018). Current research to recover positive electrode active materials are focused on leaching processes (Li et al., 2018).

The components that makeup LIBs can be generalised into two major components, leachable and non-leachable. This is based on whether it can be dissolved or deconstructed to its elemental form during leaching. The positive electrode active materials, iron, and current collectors are of the leachable components. Whereas, other components such as graphite and polymeric materials are non-leachable components. The current practice is to obtain the positive electrode active materials via manual dismantling (Chen et al., 2019; Roshanfar et al., 2019; Yu et al., 2019), which is not practical on an industrial scale. In the mechanical treatment of spent LIBs leachable contamination by iron, copper, and aluminium are expected. The

challenge in LIB recycling is to produce a positive electrode active material concentrate ($LiCoO_2$) that is suitable for the hydrometallurgical process without involving manual dismantling of LIB cell. Impurities such as iron aluminium and copper in the leach liquor can be effectively precipitated by adjusting the pH value between 4.5 (Joo et al., 2016) to 5.5 (Chen et al., 2011) using NaOH. Sa et al. (2015) argue that the removal of Cu^{2+} is more difficult than the removal of Al^{3+} and Fe^{3+} due to the higher solubility constant of Cu^{2+} and led to the study of how the presence of copper may affect the performance of $LiNi_{1/3}Mn_{1/3}Co_{1/3}O_2$ (NMC) positive electrode active materials. The results suggest that 5 wt% copper impurity is acceptable for NMC battery (Sa et al., 2015).

The mechanical treatment of LIBs has been reported to be a selective phenomenon (Widijatmoko et al., 2020). The positive and negative electrode active materials can be concentrated in the finer size region without over crushing of other battery components in both wet and dry grinding (Zhang et al., 2013). The occurrence of selective liberation can then allow size-based separation to be carried out. The sieve size of the acts as the cut point to concentrate the positive electrode active materials. The positive and negative electrode active materials are concentrated below the cut point. Whereas, the copper, aluminium, and iron are predominantly found above the cut point. To concentrate positive electrode active materials, the cut point reported varies from 250 µm (He et al., 2017) to 2000 µm (Li et al., 2009). The smaller cut point of 250 µm has been reported to give high purity of positive electrode active material, but it only recovers 56.38% $LiCoO_2$ (He et al., 2017). Moreover, the cut point size of 250 µm is substantially greater when compared to the positive electrode active materials powder size found in LIBs (1.50 µm – 7.80 µm) (Pavoni et al., 2018). This is due to the active materials are still aggregated or attached to the current collectors (Widijatmoko et al., 2020).

The occurrence of selective liberation also depends on the comminution technique being used (Hesse et al., 2017). Different techniques may result in different size distributions due to the predominant force acting during comminution as well as the milling conditions being employed (Gao and Forssberg, 1995). Selective liberation occurs when the breakage of a component is dependent on physical and mechanical properties (Mariano et al., 2016). Hesse et al. (2017) demonstrate that different predominant load being applied to a mineral would result in different liberation selectivity.

Considering the LIBs assembly, the active materials cast on the surface of current collectors can be scoured and liberated from the current collectors. Therefore, the use of liberation technique based on impact and abrasion is hypothesized to be a suitable method to promote selective libation of positive electrode active material. The use of attrition scrubbing is proposed to liberate the positive electrode active materials while minimising the breakage of copper and aluminium components.

Attrition scrubber has been designed to induce impact and shearing action between particles that promote surface abrasion and produces fine particles (Bayley and Biggs, 2005). Attrition scrubbing is conventionally used to upgrade minerals by removing surface impurities such as sand for glass making (METSO, 2018) and shown to be applicable for environmental remediation purposes such as the decontamination of storm water sediment (Petavy et al., 2009).

The original contribution of this work is related to the application of attrition scrubbing in the liberation of $LiCoO_2$ particles. The novel use of inert silica sand media as the abrasive allows the liberation $LiCoO_2$ which then allows for the concentration of $LiCoO_2$ in the finer size region. The $LiCoO_2$ product contains low copper contamination that is below the reported maximum tolerable contamination when undergoing hydrometallurgical processes. This

paper will firstly describe the cause of poor liberation of $LiCoO_2$ when using a single-stage size-reduction. The proof of concept of using attrition scrubbing as a secondary liberation technique is then discussed and the mechanism is conveyed. Additionally, the breakage kinetics of $LiCoO_2$, copper, and aluminium are studied to understand the relative breakage of different components. Finally, a demonstration for the use of electrostatic separator to recover the copper and aluminium current collector is presented.

2 Experimental

2.1 Spent LIBs sample

The spent prismatic LIBs used in this study were collected from local electronic repair shops in Ningbo, China. Only LIBs containing $LiCoO_2$ as positive electrode active materials were used. The type of positive electrode active materials was later confirmed as $LiCoO_2$ using an X-ray Diffraction (XRD, Bruker-AXS D8 Advance) and the result is presented in Figure 1.

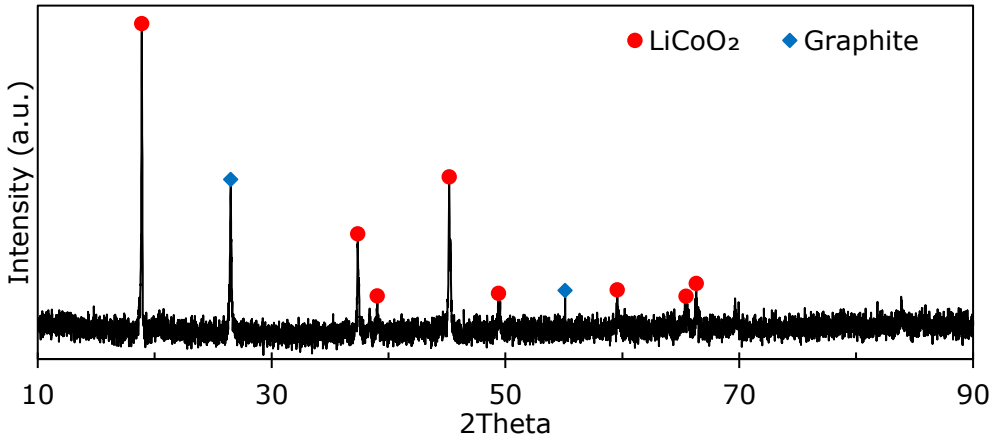

Figure 1 XRD spectra from spent LIBs. (The size fraction of < 38 µm that is later collected after sieving is tested by using an XRD and comparison is then made with $LiCoO_2$ and graphite standard powder).

All spent LIBs were firstly discharged by connecting to a 56-ohm resistor until the voltage is below 0.3 V to render them safe.

The spent LIBs were crushed using a cutting mill (Retsch SM2000) with 8 mm grid. The samples then dried in an oven at 80°C until a constant weight was achieved to remove the volatile organic electrolytes. The bulk dried sample was then split into aliquots by using a static rifle with chute size of 31 mm x 160 mm with 16 alternating chutes.

The representative samples were then screened for ferromagnetic materials by using a cylindrical rare earth magnet enclosed in polyvinyl chloride (PVC) pipe. The ferromagnetic materials were found to be less than 2 wt%.

2.2 Attrition scrubbing experiment

Attrition scrubbing experiments were carried out using a WEMCO 1L lab-scale attrition scrubber with a constant impeller speed of 1000 rpm. Clean low iron silica sand in size range of 2360 µm – 850 µm was used. In this study, the pulp density of 70 wt% with 10 wt% ratio of spent LIBs to silica sand media is used. The attrition time then varied from 2.5 min to 20 min.

Following attrition scrubbing, the product was wet sieved using 5 L water. Since the $LiCoO_2$ particles found in LIBs are in size range of 1.5 µm – 7.8 µm (Pavoni et al., 2018), a 38 µm sieve was used as the cut point. Moreover, to prevent damage to the 38 µm sieve, the attrition product was firstly sieved by using a 212 µm sieve.

Following wet sieving, the products were dried in an oven at 80^{o}C until a constant weight was achieved.

The size fraction of > 212 µm was further dry sieved into different size fractions. In this study, the attrition products were sieved into the size fraction of > 4750 µm, 4750 µm – 2360 µm and 2360 µm – 850 µm and weighted to the nearest 0.1 g. The 212 µm – 38 µm and < 38 µm product from dry sieving are combined with the dried sample from wet sieving and weighted the same way. The classified products are then analysed for elemental content.

2.3 Elemental analysis

The elemental analysis is adapted from *BS EN 62321-5:2014* (Standard, 2014). It is important that the sample tested is a representative of the entire aliquots and particle size of <250 µm is suggested in the standard. To fulfil this requirement, calcination was firstly carried for particles with a size greater than 212 µm to remove polymers that are difficult to mill. The calcination was carried out in multiple stages to prevent a sudden release of gas with the final stage at 500°C for 3 hours. The samples are allowed to cool down to room temperature and milled using a centrifugal mill (Retsch ZM200) with 0.25 mm grid. All product was sieved with a nominal aperture size of 212 µm. The size fraction of >212 µm was re-milled until the mass recovery rate of <212 µm is greater than 95 wt%. Approximately 0.2000 g ± 0.010 g of sample were weighed to four decimal places using an analytical balance.

The digestion is carried out in multiple stages of acid addition. The first stage includes 0.2 g of solid digested wit 4 ml USP grade 68 wt% HNO_3, 1 ml H_2O and 1 ml 30 wt% H_2O_2. The digestion vessels the sealed and was digested with a microwave digester (CEM MARS 5) equipped with temperature control. The microwave was set to 80 °C with a ramp time of 8 min and holding time of 2 min, followed by a further increase in temperature to 120 °C with a ramp time of 4 min and holding time of 5 min. The solution was let to cool down to a temperature below 30 °C and 4 ml of USP grade 37 wt% HCl then added and digested with the same setting previously stated. Multi-elements standard calibration curves were made by diluting and mixing different single element standard reference stock solutions (Sigma-Aldrich). The sample then analysed using an Inductively Coupled Plasma – Mass Spectrometry (ICP-MS, Nexion 300x).

2.4 Morphology observation

Scanning Electron Microscopy – Energy Dispersive X-Ray (SEM-EDX, Zeiss-Sigma-VP). The backscattered detector allows a different compound to be identified based on the average molecular weight. The heavier average molecular weight being brighter than the lighter average molecular weight. The backscattered detector was used to observe the morphological characteristics with the EDX identifies the different element present. Prior to morphological analysis, the surface is mace conductive by applying 4 nm gold layer by using gold sputtering machine (LEICA EM SCD 500).

There are currently two types of binder that are widely used; which are PVDF and SBR-CMC. The morphology analysis with EDX shows the presence of fluorine atoms and the absence of sodium atoms. This observation suggest that the binder used in positive and negative electrode is PVDF.

2.5 Electrostatic separation experiment

The electrostatic separator allows the separation of materials based on the difference in surface conductivity or by the preferential charging and attraction materials to an electric field of opposing charge potential (Kelly and Spottiswood, 1989). The electrodynamic mode involves the use of ionizing electrode and static electrode, whereby all particles receive a positive or negative charge. The separation then occurs by leakage of this assumed charge by the conductive materials compared to the retention of charge by the non-conductors. Thus, the electro-dynamic mode is able to produce fractions that concentrate non-conductive, middling, and conductive components (Kelly and Spottiswood, 1989).

Silveira et al. (2017) demonstrate that the combination of size-based separation and electrostatic separations in electro-dynamic mode allows the separation of milled LIBs components into four different product class of active materials powder, polymers, mixture (polymers and metal), and the

metallic fractions. The reported optimum parameters were initially used as a starting point and adjusted accordingly based on the visual inspection of the separated products.

In this manuscript, a roll-type electrostatic separator (Carpco, HT (15,25,36)) was used to separate the attrition products > 38 μm. The size of the static electrode is 71.5 cm X 12.5 cm X 5 cm (length x width x height), ionization electrode is a 0.010 mm wire of 10 cm in length, and roll radius of 12.7 cm. The experiment was performed at air relative humidity of 40% - 50% and temperature of 20^{o}C. The feeder vibration was maintained constant at 30% of its maximum power.

3 Results and Discussion

3.1 Characteristics of spent LIBs sample

Three representative samples that were crushed using a cutting mill only were classified. The average particle diameter (d_{50}) was found to be 1.5 mm. Each different size fraction then subjects to elemental analysis for the desired element content. The size-based recovery rate of the key elements is presented in Figure 1.

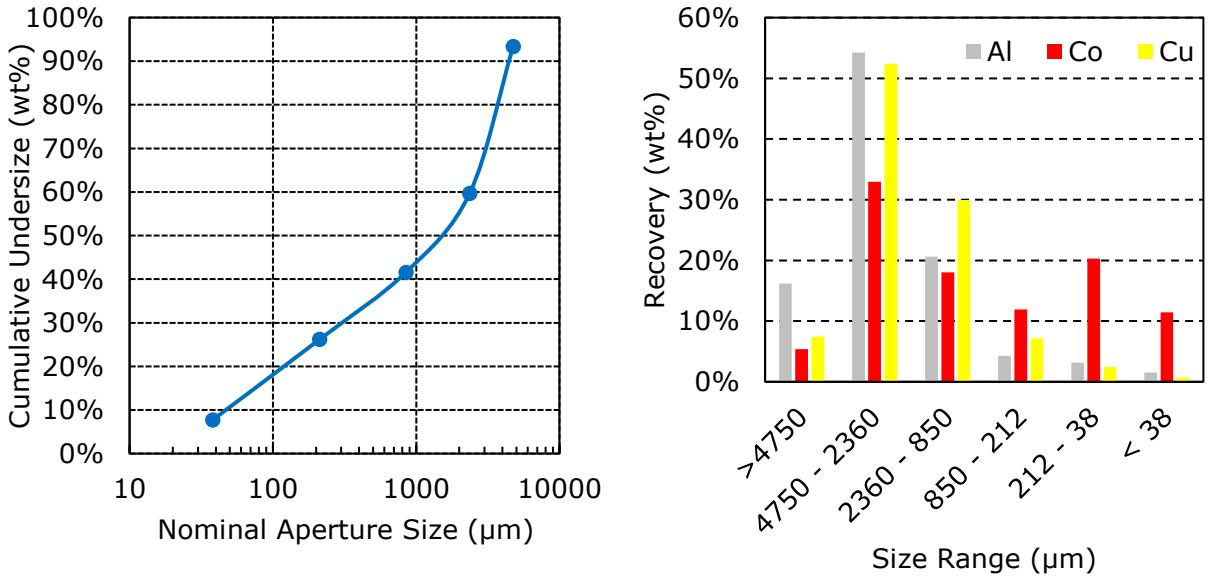

Figure 2 – The cumulative undersize semi-logarithmic pot of shredded spent LIBs and the size-recovery rate for respective size range.

Figure 2 shows that the recovery of copper and aluminium decrease as the particle size decreases. Whilst, the recovery of cobalt is dispersed throughout the various size fractions. The recovery of cobalt is higher than that of copper and aluminium below cut point 850 µm. The use of 850 µm as the cut point concentrates 43.7 wt% cobalt from the feed with the recovery of copper and aluminium of 10.3 wt% and 9.0 wt% respectively. Therefore, the size reduction of spent LIBs by using a cutting mill does induce a selective liberation of $LiCoO_2$ particles in the finer size region of < 850 µm. The occurrence of selective liberation by a cutting mill also confirms

previously published results (Wang et al., 2016). Where the smaller size fraction seems to concentrate positive electrode active materials. However, instead of $LiCoO_2$ particles being liberated by the cutting mill, the occurrence of selective liberation of $LiCoO_2$ particles is attributed by the minimum breakage of the copper and aluminium counterparts. This then results in the size fraction above the cut point 850 μm concentrates 89.7 wt% copper and 91.0 wt% aluminium with as much as 56.3 wt% of cobalt is also found in this size fraction. The reason why the single-stage liberation by using only a cutting mill is of sub-optimum is as it does not inherently liberate $LiCoO_2$ particles.

To understand the sub-optimum liberation of $LiCoO_2$ particles, the morphological observation by using SEM-EDX with a backscattered detector was carried out for the size fraction above and below 850 μm. The back scattered detector identifies different LIB components by the different contrast. The compound with heavier average molecular weight would be perceived brighter than the lighter average molecular weight. The EDX identifies the different elements present in the compound. Furthermore, the EDX can detect the presence of fluorine atoms with no sodium atom detected for the both $LiCoO_2$ and graphite laminates. Based on this observation, the binder used in the spent LIBs is deduced to be PVDF rather than SBR-CMC that contains sodium atoms.

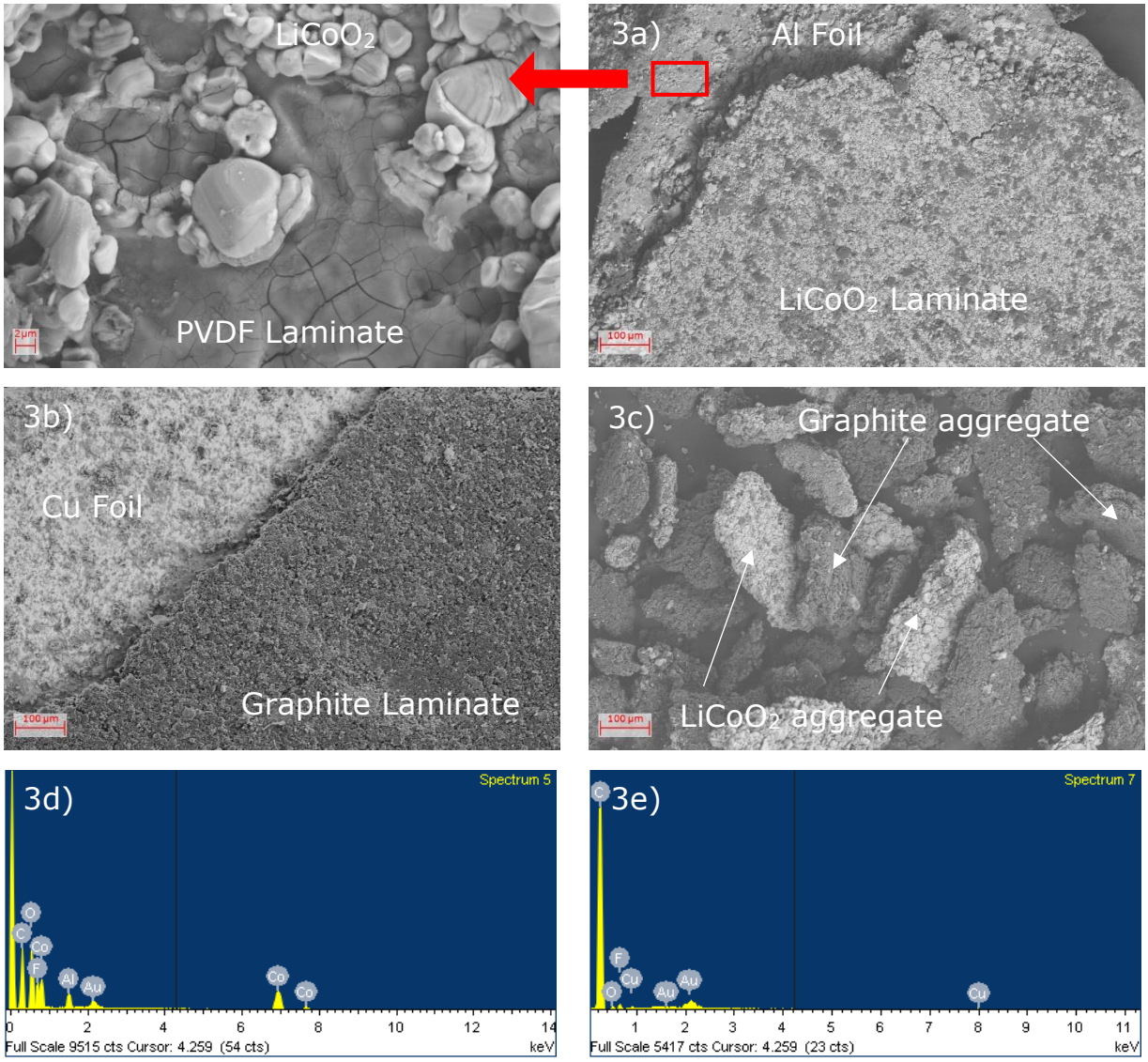

Figure 3 SEM image by using back scatted detector of 3a) Positive electrode >850 µm 3b) Negative electrode > 850 µm 3c) Powder < 850 µm 3d) XRD spectra from positive electrode 3e) XRD spectra from negative electrode.

Figure 3 shows the morphology of milled spent LIB particles above and below the 850 µm size fraction. From Figure 3a and Figure 3b, it is shown the aluminium and copper current collectors are still contaminated by the $LiCoO_2$ and graphite particles. Moreover, from Figure 3c, it can be observed that the cutting mill induces liberation of $LiCoO_2$ and graphite particles in the form of aggregates that are still held together by the PVDF binder. The $LiCoO_2$ particles are not liberated and the morphological observation

suggests that the initial liberation of spent LIBs by using a cutting mill only leads to a sub-optimum result.

3.2 Attrition liberation proof of concept

The suitability of an attrition scrubber as a second liberation stage to selectively liberate $LiCoO_2$ particles is initially measured by assessing the attrition from a short duration of 2.5 min attrition time with 70 wt% pulp density and 10 wt% of LIBs to silica sand ratio. The product was then sieved to produce different size fractions and digested for elemental analysis as previously described in the experimental method. The aluminium, cobalt, and copper elements were detected, and the size-based recovery rate is presented in Figure 4.

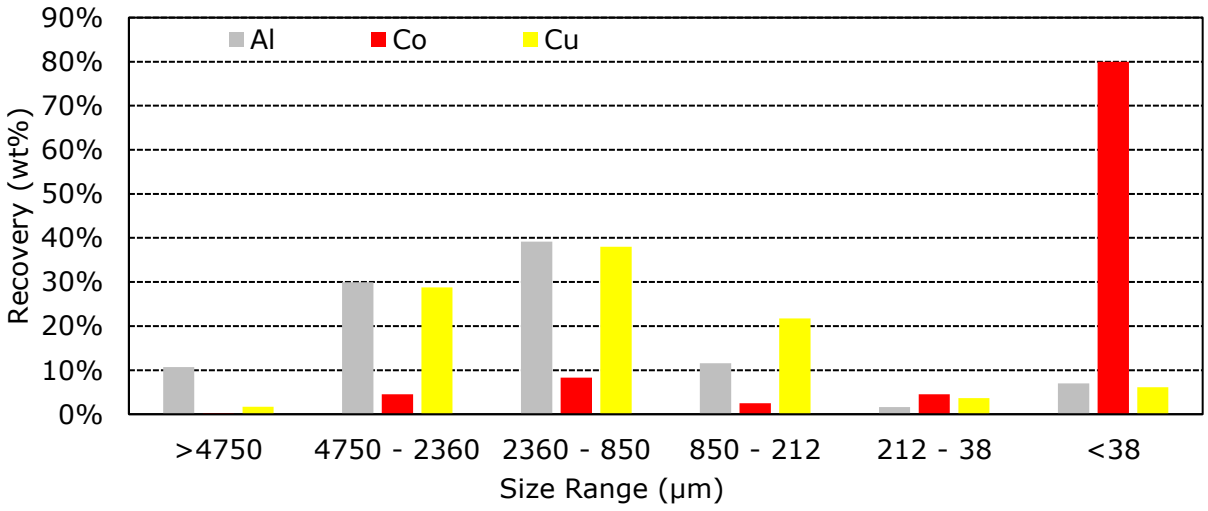

Figure 4 The size-based recovery distribution of aluminium, cobalt and copper for different size fraction after size reduction and attrition.

Figure 4 shows the size-based recovery rate of aluminium, cobalt, and copper after attrition. Comparing the result of size-based recovery distribution for the sample before (Figure 2) and after (Figure 4) attrition, the copper and aluminium components are still dispersed in the size fraction of > 38 μm. However, cobalt has a much higher recovery rate increase in the size fraction of < 38 μm from 11.4 wt% to 80.0 wt%. From Figure 4, the

size fraction of < 38 µm recovers 7.0 wt% aluminium and 6.1 wt% copper. The majority of the copper and aluminium can be found in the size fraction of > 38 µm. The results indicate that attrition scrubbing allows the selective liberation of $LiCoO_2$ particles.

In order to quantify the degree of improvement of selective liberation, the Fuerstenau upgrading curve in a recovery plot for the classified comminution product in percentage finer is used (Hesse et al., 2017). To plot the Fuerstenau recovery plot, the desired (valuable) component and undesired (waste) is firstly defined. In this case, the valuable component is cobalt with the waste components of copper and aluminium. The cumulative recovery of valuable and waste with increasing cut point size is plotted in the same graph. By this way, the selective liberation of cobalt, copper, and aluminium can be determined. Moreover, by taking the aluminium as valuable and copper as waste, the selective liberation occurrence between the two can also be assessed.

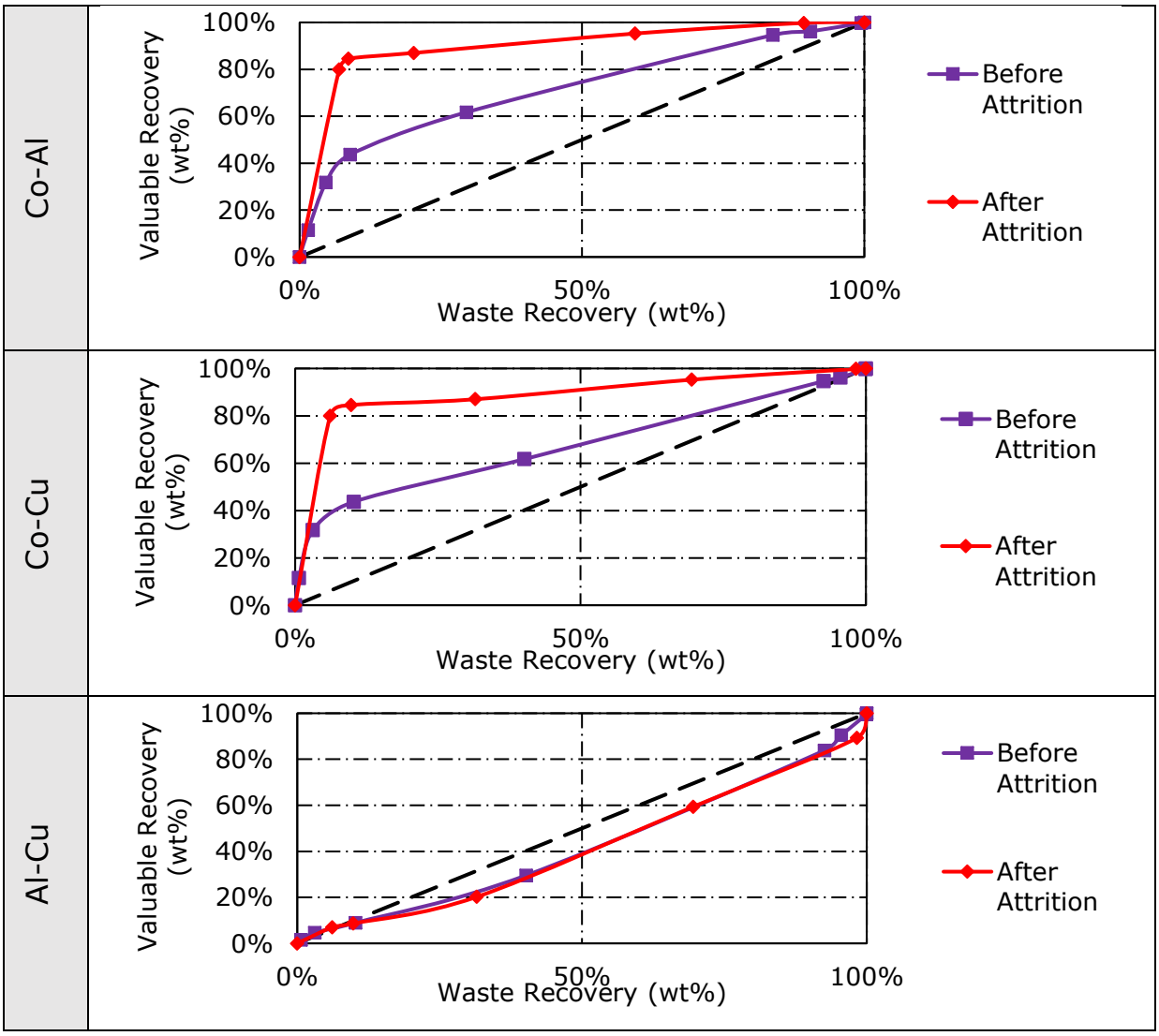

Figure 5 Fuerstenau recovery curves comparison before and after attrition.

Figure 5 presents the comparison of selective liberation in the form of Fuerstenau recovery curves for the cobalt-aluminium (Co-Al), cobalt-copper (Co-Cu), and aluminium-copper (Al-Cu). In a Fuerstenau recovery curve plot, the selective comminution product is always separated into two fractions of the fine and coarse fraction. When the plot of the cumulative valuable and waste is of a diagonal line, it indicates that there is no selective liberation. A recovery curve above the diagonal line indicates that the valuable component is selectively liberated in the finer size region.

Otherwise, the recovery curve below the diagonal line indicates the enrichment of valuable component in the bigger size fraction.

From Figure 5, the first stage of liberation using a cutting mill does induce selective liberation of cobalt in the finer size region. The result suggests that selective liberation of $LiCoO_2$ in the finer size region is improved using an attrition scrubber. This is indicated by the recovery line of Co-Al and Co-Cu that are further from the diagonal following attrition. Furthermore, the Fuerstenau plot which takes account of the interaction between aluminium and copper (Al-Cu) is also shown in Figure 5 indicates that the aluminium is concentrated in the larger size fraction relative to copper.

From the Al-Cu plot shown in Figure 5, the result suggests that there is a minimum improvement in the enrichment of the two components based on size. Therefore, the use of size-based separation to separate copper and aluminium is a challenging task.

Table 1 Comparison of selective liberation efficiency before and after attrition

Recovery Line	Selective Liberation Efficiency					
	1st Stage		2nd Stage		Change	
	a.u.	%	a.u.	%	a.u.	%
Co-Al	0.21	42.7	0.40	79.3	0.18	36.6
Co-Cu	0.17	34.4	0.38	77.0	0.21	42.6
Al-Cu	0.07	14.3	0.08	16.5	0.01	2.2

The selective liberation improvement employing attrition scrubber as the second stage can quantified by measuring the area bound by the recovery line and the diagonal line. It is important to point out that the area of 0.50 arbitrary unit (a.u.) between the recovering line and diagonal line is the highest area achievable if perfect separation has occurred. In this discussion, the integration is carried using the trapezium method. The results are presented as selective liberation efficiency %; that is the area bound by the

recovery line and the diagonal line divided by 0.50 a.u. and summarised in Table 1.

From the results presented in Table 1, the initial liberation using only a cutting mill does induce a degree of selective liberation of cobalt towards aluminium and copper by 42.7 % and 34.4 %respectively. Attrition scrubbing as the second stage of liberation improves the selective liberation of cobalt towards aluminium and copper by 36.6 % and 42.6 % respectively. There is only a slight increase in the selective liberation efficiency between aluminium and copper by 2.2 %. Thus, the separation of aluminium and copper based on size for attrition scrubbing product is still unlikely.

From the proof of concept laid out, the initially sub-optimum liberation of $LiCoO_2$ particles using cutting mill only can be further improved by the use of attrition scrubbing as a second stage for liberation. The attrition products concentrate the majority of $LiCoO_2$ particles in the fine size region of less than 38 µm in 2.5 min attrition time. Furthermore, it is also expected that the graphite is also concentrated together with the $LiCoO_2$ particles due to the weaker attachment of graphite laminate onto the copper current collector as compared to the $LiCoO_2$ laminate counterparts (Dai et al., 2019). This weaker attachment of the negative electrode active materials may also help to explain the Fuerstenau Al-Cu curve that is below the diagonal line. The $LiCoO_2$ laminate may help in maintaining the aluminium current collector shape and preventing further breakage. Whereas, the copper current collector may not have this benefit.

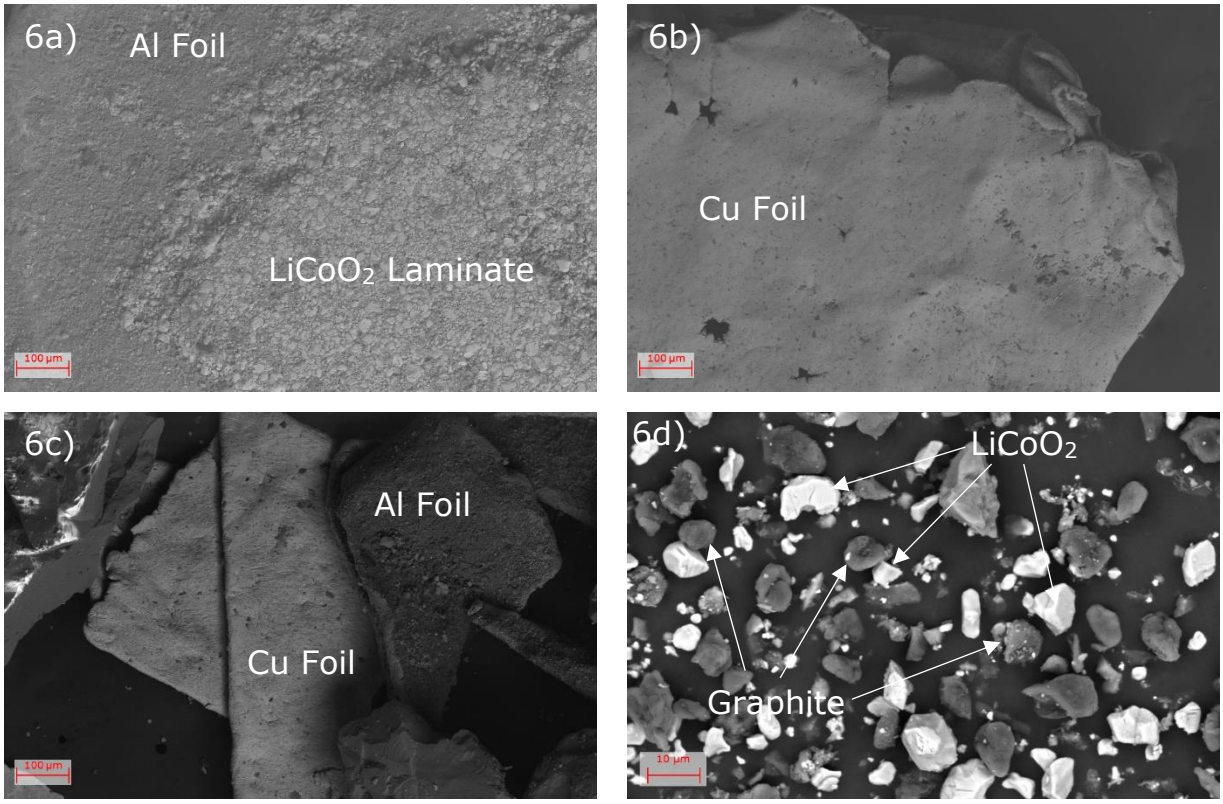

Figure 6 SEM image after 2.5 min attrition time by using back scatted detector of 6a) Positive electrode >850 µm 6b) Negative electrode > 850 µm 6c) Powder 850 µm - 212 µm 6d) Powder < 38 µm.

Morphology observation of attrition product is presented in Figure 6. The weaker attachment of graphite towards copper current collector as compared to the aluminium counterparts can be clearly seen by comparing Figure 6a to Figure 6b. The copper current collector is relatively cleaner than that of the aluminium counterpart. Figure 6c shows clean copper and aluminium in the size fraction of 850 µm – 212 µm. This results from the breakage of copper and aluminium from the size fraction > 850 µm after 2.5 min attrition time. Furthermore, the initially aggregated $LiCoO_2$ particles are no longer can be found in this size fraction. Instead, the particles have been disaggregated into the size fraction of < 38 µm as observed in Figure 6d. Moreover, the copper and aluminium components were not observed in Figure 6d and suspected to break into fine particles and contaminate the surface of the larger particles.

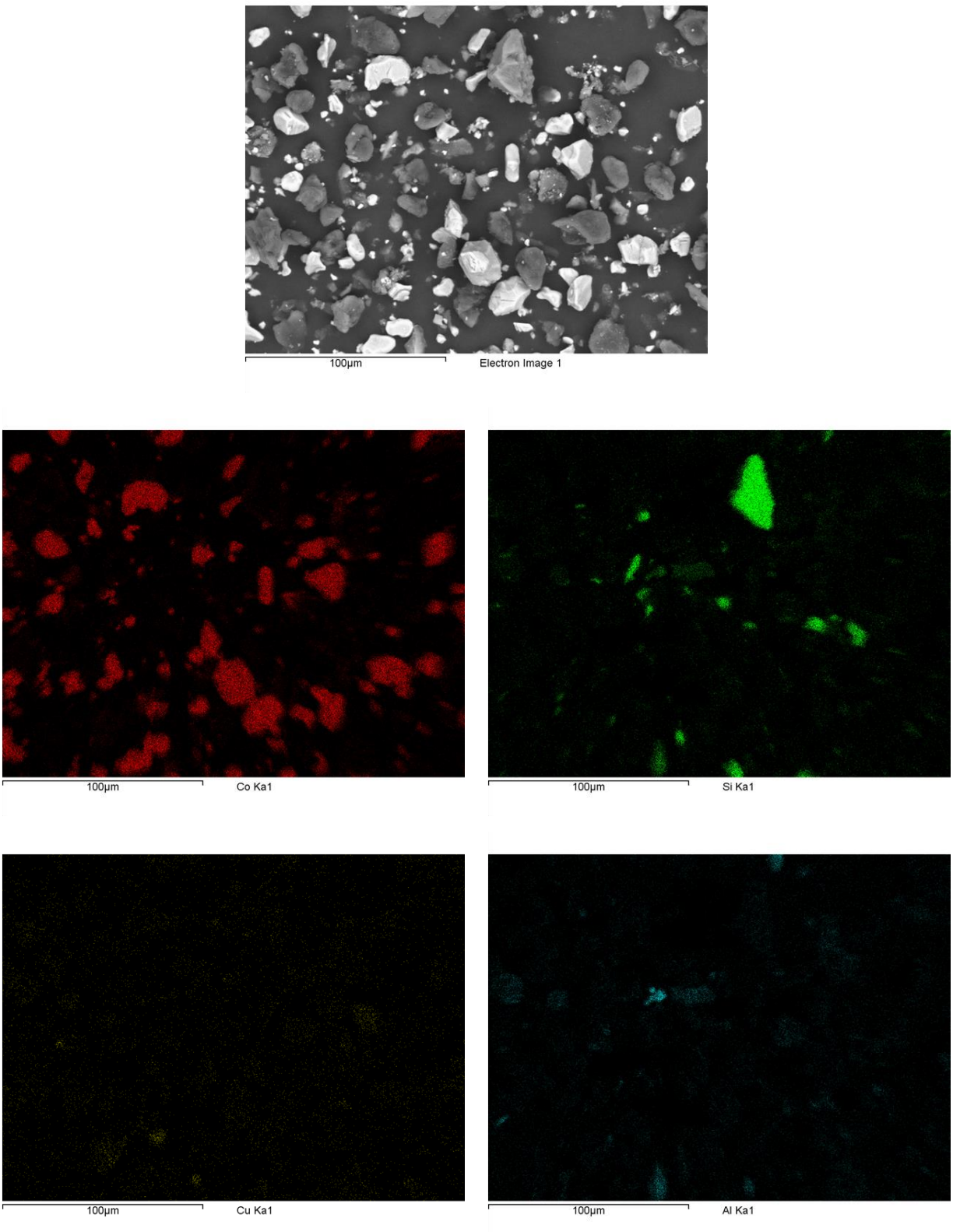

Figure 7 EDX-Elemental mapping of 2.5 min < 38 µm attrition product.

To confirm that the copper and aluminium contaminating the surface of the larger particles, elemental mapping by using EDX was carried out for the attrition product of < 38 μm. The EDX-elemental mapping was set to detect the cobalt, silica, copper and aluminium elements and the results of the elemental mapping is presented in Figure 7. From the observation, it was found that some of the graphite, $LiCoO_2$ and SiO_2 particles are contaminated by copper and aluminium fine particles. From the elemental mapping results, it is understood that further mechanical separation of copper and aluminium from this powder may be challenging.

Comparing the particle morphology of before and after attrition, the impact and shearing load appears to liberate the active materials that laminate the positive and negative electrodes. The impact load causes the disaggregation of $LiCoO_2$ and graphite and is concentrated in the size fraction < 38 μm and scours the particles from the aluminium and copper current collectors. The size fraction of 850 μm - 212 μm does not initially have clean copper and aluminium. However, after attrition, clean copper and aluminium can be found in this region. Thus, the liberation of $LiCoO_2$ and graphite particles also followed by the breakage of copper and aluminium. The breakage of copper and aluminium current collector is deduced to be slower than that of the active materials. To confirm this, the study related to the breakage kinetics of $LiCoO_2$ laminate as compared to the copper and aluminium current collector was carried out.

3.3 The breakage kinetics and its implication

The pulp density and the LIBs to silica sand ratio were kept constant at 70 wt% and 10 wt% respectively. Samples from the size fractions 4750 μm – 2360 μm, 2360 μm – 850 μm, 850 μm – 212 μm, 212 μm – 38 μm, and < 38 μm with different attrition time is analysed for aluminium, cobalt, and copper. The comparison of breakage kinetics can then be made for different components of spent LIBs. Breakage kinetics of wet and dry grinding has

been reported to be a first-order (Sadler III et al., 1975). The rate of disappearance, by breakage, from a given narrow size, is given by Equation 1.

$$\frac{dw}{dt} = -kw \qquad \text{Equation 1}$$

Where w is the weight of material in the given size fraction, t is time, and k is milling rate constant for the given size fraction. k is, in general, different for each size fraction present and is dependent on operating parameters, mill design, the material being milled, and the environment inside the mill.

Equation 1 may be integrated to give Equation 2.

$$w = w_o e^{-kt} \qquad \text{Equation 2}$$

Where w_o is the initial amount of material present in the specific size range. Equation 2 suggests that a plot of ln w versus t should be a straight line with ordinate intercept ln w_o and slope equal to –k.

Two cut points of 2360 µm and 38 µm are assessed to compare the breakage kinetics.

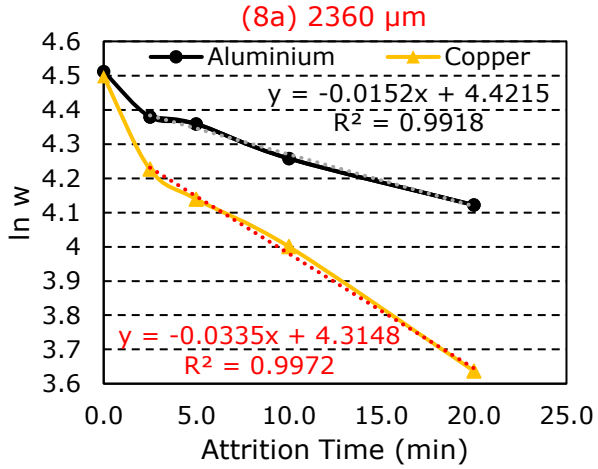

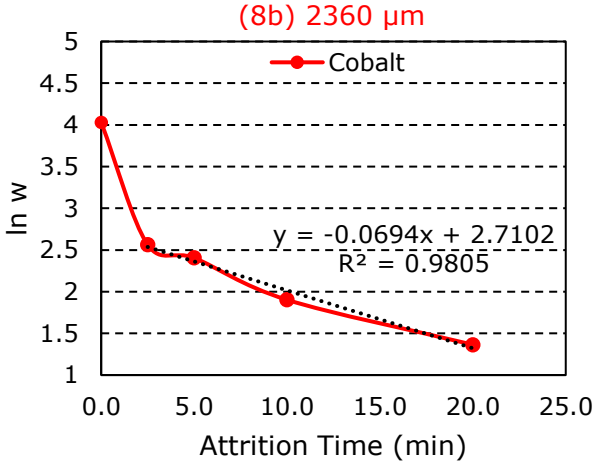

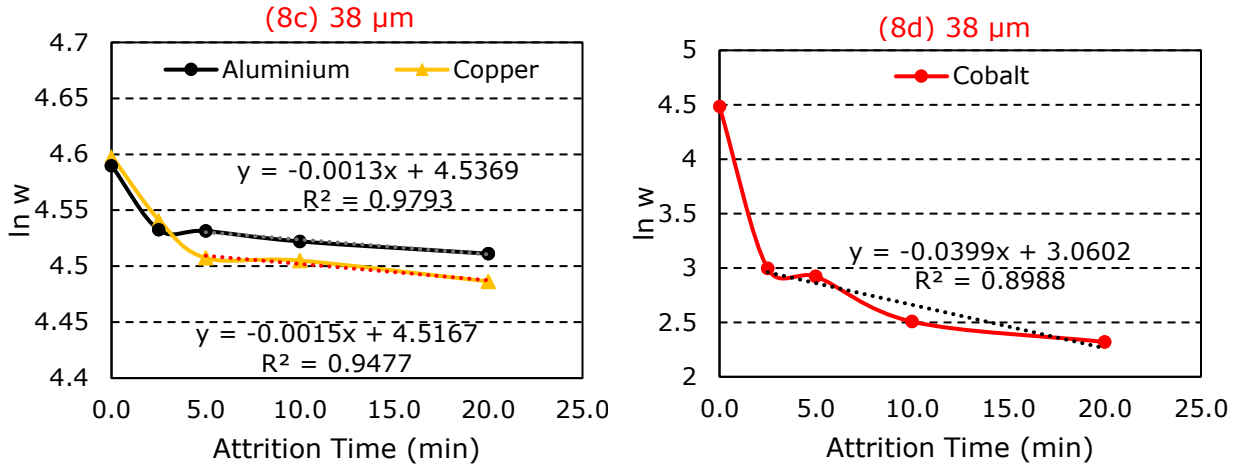

Figure 8 The breakage kinetics of aluminium, copper, and $LiCoO_2$ laminate (cobalt) for less than 2360 µm and 38 µm.

From Figure 8, in the initial phase, the breakage kinetics of aluminium, copper, and cobalt does not initially follow the first-order breakage kinetics for both the 2360 µm and 38 µm cut point. This is ignored when calculating the brekage kinetics. The breakage rate comparison of aluminium, copper and cobalt is calculated using the linear region. Therefore, in this study, the breakage kinetics were calculated using the points after initial breakage.

From Figure 8a, by comparing the aluminium and copper breakage gradient, it can be seen that the aluminium component experiences a slower breakage rate than that of the copper component. This can be explained via the copper foil mechanical degradation after the battery is being cycled that makes copper mechanically weaker than aluminium. The weaker attachment of graphite laminate on to copper than that of $LiCoO_2$ laminate on to aluminium may also help to explain this phenomenon. The copper became more susceptible to breakage by the attrition media as compared to the aluminium foil that is more protected by the $LiCoO_2$ laminate.

Figure 8b shows the breakage kinetics of the $LiCoO_2$ particles via the detection of cobalt through the cut point 2360 µm. Comparing the gradient of $LiCoO_2$ laminate breakage kinetic to that of aluminium and copper, it can

be seen that the $LiCoO_2$ laminate breaks at a faster rate than that of copper and aluminium. This also implies that the liberation of $LiCoO_2$ particles is required prior to the breaking of the aluminium. Hence, this also confirms that the $LiCoO_2$ laminate prevents the breakage of the aluminium component.

The breakage kinetics of aluminium and copper passing through the cut point of 38 µm is presented in Figure 8c. Similarly, to the phenomenon described for Figure 8a, the aluminium breaks slower than that of copper.

From Figure 8d, it can be seen that the $LiCoO_2$ laminate breakage rate towards the cut point of 38 µm is faster than that of copper and aluminium. The gradient of the cobalt breakage kinetics is much higher than that of copper and cobalt. The substantially faster breakage of $LiCoO_2$ laminates towards the cut point of less than 38 µm is expected. The $LiCoO_2$ particle size range found in spent LIBs is between 1.50 µm – 7.80 µm (Pavoni et al., 2018). This indicates that the liberation of $LiCoO_2$ particles that are still held together by the binder is much faster than the fines produced by the breakage of aluminium and copper.

The comparison of the breakage kinetics of aluminium, copper and $LiCoO_2$ laminate shows that the $LiCoO_2$ laminate breaks faster than that of copper and aluminium. The faster rate of $LiCoO_2$ laminate shows that it is selectively liberated during attrition. Moreover, the copper component breaks faster than the aluminium component. These may be caused by the following factors:

- The copper and aluminium foils in the bigger size fraction are still coated by the active materials and thus resulting in the liberation of active material laminates prior to the breakage of the copper and aluminium component during attrition.

- The weaker attachment of graphite lamination on to copper current collector is than that of $LiCoO_2$ lamination on to aluminium. Moreover, as the battery is cycled, the mechanical properties of copper degrade more severely than the aluminium counterparts. These helps explain the faster breakage rate of copper when compared to aluminium.
- The $LiCoO_2$ laminate is held together by PVDF binder that has weaker mechanical properties than that of copper and aluminium. The copper and aluminium foil has higher tensile strength than PVDF (Butt et al., 2016; Group, 2011). As a result, the $LiCoO_2$ particles are being disaggregated and thus resulting in faster liberation rate as compared to the copper and aluminium counterparts. This effect is more apparent for the breakage rate of cobalt in comparison with copper and aluminium into the size fraction of less than 38 µm.

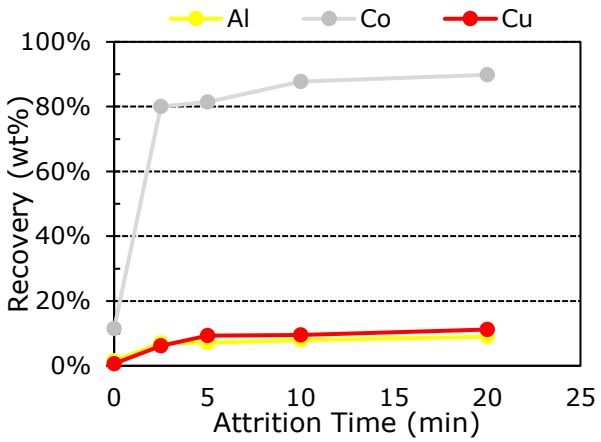

Figure 9 Recovery rate of aluminium, $LiCoO_2$ (cobalt) and copper in the size fraction of less than 38 µm with varying attrition time.

Figure 9 presents the recovery rate of aluminium, cobalt and copper concentrated in the size fraction of less than 38 µm. From Figure 9, LiCoO2 has the highest recovery rate compared to copper and aluminium. The increase recovery of $LiCoO_2$ particles also followed by the decrease in $LiCoO_2$ grade. With the assumption that the graphite is liberated with the same degree than that of $LiCoO_2$ particle and the ratio of $LiCoO_2$ to graphite is

constant. The concentration of the graphite particles in the size fraction < 38 μm is calculated based on the ratio of cobalt to graphite in $LiCoO_2$ batteries from the published data by (Wang et al., 2016). By this way, the concentration of the silica sand in the < 38 μm attrition product can also be estimated and summarised in Table 2.

Table 2 Composition of attrition products following attrition against time.

Attrition Time (min)	Concentration (wt%)				
	Al	$LiCoO_2$	Cu	Graphite	Sand
0.0	1.6	60.7	0.8	36.9	0.0
2.5	0.8	48.7	1.0	39.1	10.4
5.0	0.8	45.6	1.3	36.7	15.6
10.0	0.9	44.6	1.3	35.9	17.4
20.0	0.9	40.9	1.3	32.9	23.9

From Table 2, despite the increase in recovery of $LiCoO_2$ particles as attrition time increases, the $LiCoO_2$ grade decreases as the attrition time increases. This is attributed to the contamination caused by the silica sand media as attrition time increases. This is caused following the breakage of silica particles. The contamination from the attrition media is expected, and low iron silica sand has been chosen for it is chemically resistance to the lixiviant which has been proposed by researchers to leach the $LiCoO_2$ particles. Therefore, the main leachable contamination of attrition products is copper and aluminium. From previously reported literature, a proportion of 5 wt% copper relative to $LiCoO_2$ is a tolerable contamination for leaching and resynthesizing (Sa et al., 2015). Aluminium can initially be removed via dissolution by using NaOH. From Table 2, the 20 min attrition time results in only 3 wt% copper relative to $LiCoO_2$. Therefore, the attrition product can be concluded to be suitable for subsequent hydrometallurgical processes.

Remaining graphite can be separated from silica sand by using froth flotation due to the hydrophilicity difference (i.e. graphite is hydrophobic and silica sand is hydrophilic) (Lu and Forssberg, 2001).

Diekmann et al. (2017) have proposed a second stage liberation by using a cutting mill, the active material fine particles concentrate were recovered by using air classifier, this method resulted in 75% recovery. Comparing the method proposed, higher recovery rate of active materials from second stage wet liberation by using an attrition scrubbing can be found 80.0 wt% - 89.8 wt%. Moreover, the use of air classifier to recover spent LIBs active materials may impose serious hazard related to respiratory health.

3.4 The separation of attrition scrubber > 38 µm product

The majority of the $LiCoO_2$ particles are concentrated in the size fraction of less than 38 µm. The size fraction > 38 then concentrates the copper and aluminium current collectors. The > 38 µm sample obtained then subject to the electrostatic separation to separate polymer, silica sand and the current collector. A roll-type electrostatic separator (Carpco, HT (15,25,36)) was used in this study.

The electrostatic separator comprises of two main components which are the beam and static electrode. The ionizing electrode pinned nonconductive materials on to the roll and collected at the end of the roll by a static brush. For the particles that are heavier than the pinning action are collected as middlings. The static electrode attracts conductive materials while leaving the non-conductive to fall through the roll and collected. Considering the composition of the sample, both electrodes were used to separate the sample into three different fractions, such that the polymeric separator and fine silica sand would be pinned on to the roll and collected on the left hand side of the receptacle, the voltage is adjusted so that the silica sand > 850 µm would not be pinned as strongly as the polymeric separator and collected

as middling, and the conductive materials are thrown into the right side of the receptacle.

The optimum conditions reported by Silveira et al. (2017) were initially used and need to be adjusted for a workable parameter. The particles were flowing unevenly and arching between the electrodes towards copper and aluminium foils was observed. Moreover, that the silica sand with particle size of > 850 μm was strongly pinned onto the roll and can be found in the non-conductor fraction. To overcome these issues, adjustment trial and error based on visual inspection was carried out to adjust the parameters and minimise these issue. The key parameters of the electrostatic separator are shown in Table 3.

Table 3 Parameters set for the electrostatic separator

Parameters	Silveira et al. (2017)	Adjusted Value
Roll Speed (RPM)	20	50
Electrode Voltage (kV)	25	20
d1-Ionization Electrode Distance (cm)	6	5
d2-Static Electrode Distance (cm)	6	8
θ_1 (°)	25	35
θ_2 (°)	75	65
Deflector I Angle (°)	N/A	50
Deflector II Angle (°)	N/A	35

The deflector angle I and II were kept constant at 50° and 35° respectively. The roll speed was initially 20 rpm and adjusted to 50 rpm to make the particle flows evenly. After adjusting the roll speed, the arching from the ionization electrodes to the copper and aluminium foils are still observed, the

electrode voltage is then reduced from 25kV to 20kV. The decrease in electrode voltage also causes the larger silica sand > 850 μm to be less strongly pinned on to the roll and less lifting action for the copper and aluminium foils. This then result in LIB separator found as middling and copper and aluminium foils were observed to falls together with the silica sand. The ionization electrode is then moved closer to the roll from 6 cm to 5 cm and cause more separator pinned onto the roll. However, visual inspection reveals that the copper and aluminium foil is visually flowing together with the silica sand. The distance between the ionisation electrode and the feeder (θ_1) was adjusted from 25^o to 35^o. This is done to extend the charging time for the particles to acquire charge. However, keeping the distance between the two electrodes constant seems to do not allow enough residence time for the copper and aluminium foils to undergoes charge reversal that is sufficient to lift the particles. The distance between the two electrodes was made narrower and adjusted from 50^o to 40^o (from θ_2=75^o to θ_2=65^o). After adjusting the ionizing and static electrode angle, the copper and aluminium is lifted and hitting the static electrode. Therefore, the static electrode (lifting electrode) is moved further from the roll to minimise the electrode getting hit by the copper and aluminium foils.

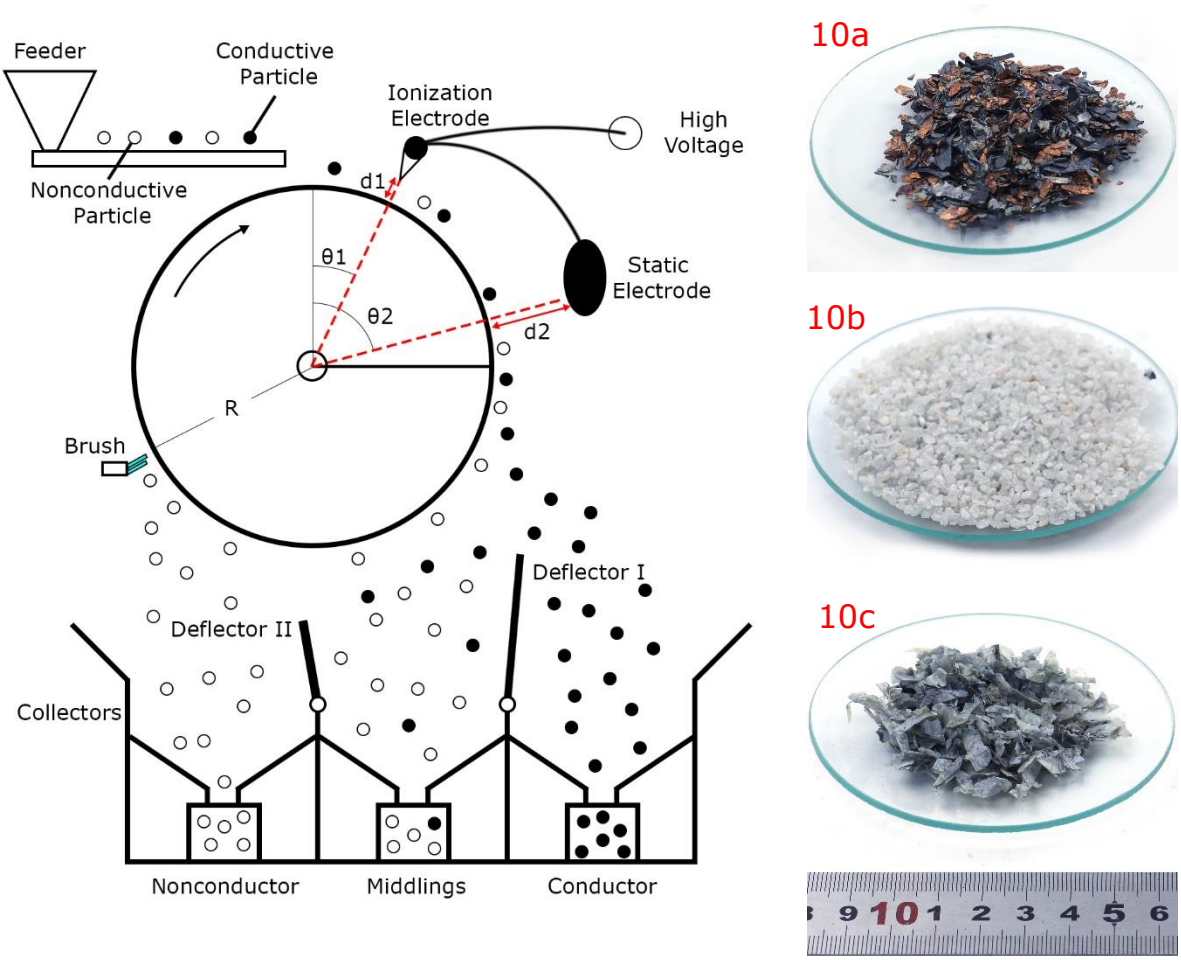

Figure 10 Schematic diagram of an electrostatic separator and the resulting products; 10.a – Conductor, 10b - Middlings, 10c - Non-conductor.

In a one-pass electrostatic separation, only copper and aluminium foils are registered as a conductive fraction. However, it was observed that the middling still contains a substantial amount of conductor materials and therefore the middling was re-introduced into the feeder. The middling was re-introduced to the feeder for five times. To assess the grade of the resulting separation, manual picking was done. The schematic diagram of the electrostatic separator, as well as the resulting separated products, are shown in Figure 10. The conductive fractions obtained (Figure 10a) were of 97.65 wt% metal, the impurities came from the short-circuiting of the silica sand from the middling. The middling obtained (Figure 10b) contain 99.01 wt% silica sand with small impurities from the copper and aluminium current

collector. The nonconductive (Figure 10c) obtained contains 95 v% (14.87 wt%) battery separator, with the main contamination from the fine (< 850 μm) silica sand.

The results from this exploratory study suggest that electrostatic separator is a useful technique in separating the current collectors and polymeric materials from the attrition media. It is also observed that the attrition media that has undergone size reduction < 850 μm are registered as nonconductive and collected together with the polymeric materials. The recovered attrition media are visually clean from the separator and with minimum contamination from copper and aluminium, and therefore can be re-used for the subsequent attrition media.

4 Conclusion

Mineral processing technique is an important part in LIBs recycling to liberate and concentrate valuable metals due to its high throughput (Al-Thyabat et al., 2013). The recovery technique proposed in this research allows the majority of $LiCoO_2$ particles to be recovered in the size fraction of < 38 μm with minimum contamination from copper and aluminium components and therefore reducing the need for leachate purification during hydrometallurgical process. This is achieved by using attrition scrubbing as the second stage of liberation.

From the morphological analysis of particles before attrition, above and below cut point of 850 μm shows a distinct difference. Above the cut point 850 μm, the $LiCoO_2$ particles are still laminating the aluminium current collector. Whereas, below the cut point 850 μm, the $LiCoO_2$ particles are in the form of aggregate. Based on this observation, two cut points of 2360 μm and 38 μm were selected. The cut points selected in order to study the different breakage rate for delamination (2360 μm) and deaggregation (38 μm) of $LiCoO_2$ particles. The breakage kinetics of $LiCoO_2$ particles for cut

point 2360 μm is faster than that of cut point 38 μm. This indicates the delamination is faster than the deaggregation of $LiCoO_2$ particles. Moreover, the results show that the breakage rate follows the order of $LiCoO_2$>Cu>Al for both cut points. This result indicates that the $LiCoO_2$ delamination and disaggregation is faster than the breakage of the copper and aluminium foil. This then results in 89.8 wt% $LiCoO_2$ recovery with minimum 9.0 wt% aluminium and 11.2 wt% copper recovery within 20 min attrition time.

The use of attrition scrubbing as a second stage liberation technique has been proposed to concentrate $LiCoO_2$. Moreover, the copper and aluminium can be recovered by using electrostatic separator. However, the technique proposed is still carried out in a lab-scale and have not yet been tested in a pilot-scale and is the main drawback of the proposed study. Future work should include the scaling up of attrition scrubbing.

Acknowledgement

The authors are grateful for the support from New Material Institute, The University of Nottingham Ningbo China. The authors are also grateful for the help in assembling the equipment Ivena Wiranata, Wilsen Kusuma, and Ryan Jonathan.

This work is financially supported by the Innovation Team of Ningbo Science and Technology Bureau (2011B81006), Industrial Technology Innovation and Industrialization of Science and Technology Project (2014A35001-2), Ningbo Natural Science Foundation of Ningbo Science and Technology Bureau (2017A610136), Chinese Science and Technology Support Plan Project (2015BAF04B01-2), and Green Manufacturing System Integration Project 2016 of Chinese Ministry of Industry and Information.

References

Al-Thyabat, S., Nakamura, T., Shibata, E., Iizuka, A., 2013. Adaptation of minerals processing operations for lithium-ion (LiBs) and nickel metal hydride (NiMH) batteries recycling: Critical review. Minerals Engineering 45, 4-17. 10.1016/j.mineng.2012.12.005
Bayley, R.W., Biggs, C.A., 2005. Characterisation of an attrition scrubber for the removal of high molecular weight contaminants in sand. Chemical Engineering Journal 111(1), 71-79. 10.1016/j.cej.2005.05.009
Blomgren, G.E., 2017. The Development and Future of Lithium Ion Batteries. Journal of The Electrochemical Society 164(1), A5019-A5025. 10.1149/2.0251701jes]
Butt, J., Mebrahtu, H., Shirvani, H., 2016. Microstructure and mechanical properties of dissimilar pure copper foil/1050 aluminium composites made with composite metal foil manufacturing. Journal of Materials Processing Technology 238, 96-107. 10.1016/j.jmatprotec.2016.07.014
Chen, L., Tang, X., Zhang, Y., Li, L., Zeng, Z., Zhang, Y., 2011. Process for the recovery of cobalt oxalate from spent lithium-ion batteries. Hydrometallurgy 108(1-2), 80-86. 10.1016/j.hydromet.2011.02.010
Chen, X., Kang, D., Cao, L., Li, J., Zhou, T., Ma, H., 2019. Separation and recovery of valuable metals from spent lithium ion batteries: Simultaneous recovery of Li and Co in a single step. Separation and Purification Technology 210, 690-697. 10.1016/j.seppur.2018.08.072
Dai, C., Wang, Z., Liu, K., Zhu, X., Liao, X., Chen, X., Pan, Y., 2019. Effects of cycle times and C-rate on mechanical properties of copper foil and adhesive strength of electrodes in commercial LiCoO2 LIBs. Engineering Failure Analysis 101, 193-205. 10.1016/j.engfailanal.2019.03.015
Diekmann, J., Hanisch, C., Froböse, L., Schälicke, G., Loellhoeffel, T., Fölster, A.-S., Kwade, A., 2017. Ecological Recycling of Lithium-Ion Batteries from Electric Vehicles with Focus on Mechanical Processes. Journal of The Electrochemical Society 164(1), A6184-A6191. 10.1149/2.0271701jes
Dunn, B., Kamath, H., Tarascon, J.-M., 2011. Electrical energy storage for the grid: a battery of choices. Science 334(6058), 928-935.
Gaines, L., 2018. Lithium-ion battery recycling processes: Research towards a sustainable course. Sustainable Materials and Technologies 17, e00068. 10.1016/j.susmat.2018.e00068
Gao, M., Forssberg, E., 1995. Prediction of product size distributions for a stirred ball mill. Powder Technology 84(2), 101-106.
Group, Q., 2011. Technical Data Sheet for Polyvinylidene Rod & Sheet. Quadrant Group.
He, Y., Zhang, T., Wang, F., Zhang, G., Zhang, W., Wang, J., 2017. Recovery of LiCoO2 and graphite from spent lithium-ion batteries by Fenton reagent-assisted flotation. Journal of Cleaner Production 143, 319-325. 10.1016/j.jclepro.2016.12.106

Hesse, M., Popov, O., Lieberwirth, H., 2017. Increasing efficiency by selective comminution. Minerals Engineering 103-104, 112-126. 10.1016/j.mineng.2016.09.003
Joo, S.-H., Shin, D., Oh, C., Wang, J.-P., Shin, S.M., 2016. Extraction of manganese by alkyl monocarboxylic acid in a mixed extractant from a leaching solution of spent lithium-ion battery ternary cathodic material. Journal of Power Sources 305, 175-181. 10.1016/j.jpowsour.2015.11.039
Kelly, E., Spottiswood, D., 1989. The theory of electrostatic separations: A review Part I. Fundamentals. Minerals Engineering 2(1), 33-46.
Li, J., Shi, P., Wang, Z., Chen, Y., Chang, C.C., 2009. A combined recovery process of metals in spent lithium-ion batteries. Chemosphere 77(8), 1132-1136. 10.1016/j.chemosphere.2009.08.040
Li, L., Zhang, X., Li, M., Chen, R., Wu, F., Amine, K., Lu, J., 2018. The Recycling of Spent Lithium-Ion Batteries: a Review of Current Processes and Technologies. Electrochemical Energy Reviews 1(4), 461-482. 10.1007/s41918-018-0012-1
Lu, X., Forssberg, E., 2001. Flotation selectivity and upgrading of Woxna fine graphite concentrate. Minerals engineering 14(11), 1541-1543.
Mariano, R.A., Evans, C.L., Manlapig, E., 2016. Definition of random and non-random breakage in mineral liberation - A review. Minerals Engineering 94, 51-60. 10.1016/j.mineng.2016.05.005
METSO, 2018. Basics in Minerals Processing, 11 ed.
Pavoni, F.H., Sita, L.E., dos Santos, C.S., da Silva, S.P., da Silva, P.R.C., Scarminio, J., 2018. LiCoO2 particle size distribution as a function of the state of health of discarded cell phone batteries. Powder Technology 326, 78-83. 10.1016/j.powtec.2017.12.059
Petavy, F., Ruban, V., Conil, P., Viau, J.Y., 2009. Attrition efficiency in the decontamination of stormwater sediments. Applied Geochemistry 24(1), 153-161. 10.1016/j.apgeochem.2008.09.014
Richa, K., Babbitt, C.W., Gaustad, G., Wang, X., 2014. A future perspective on lithium-ion battery waste flows from electric vehicles. Resources, Conservation and Recycling 83, 63-76. 10.1016/j.resconrec.2013.11.008
Roshanfar, M., Golmohammadzadeh, R., Rashchi, F., 2019. An environmentally friendly method for recovery of lithium and cobalt from spent lithium-ion batteries using gluconic and lactic acids. Journal of Environmental Chemical Engineering 7(1), 102794. 10.1016/j.jece.2018.11.039
Sa, Q., Heelan, J.A., Lu, Y., Apelian, D., Wang, Y., 2015. Copper Impurity Effects on LiNi(1/3)Mn(1/3)Co(1/3)O2 Cathode Material. ACS Appl Mater Interfaces 7(37), 20585-20590. 10.1021/acsami.5b04426
Sadler III, L.Y., Stanley, A.D., Brooks, D.R., 1975. Attrition mill operating characteristics. Powder Technology 12(1), 19-28. doi.org/10.1016/0032-5910(75)85004-2

Silveira, A.V.M., Santana, M.P., Tanabe, E.H., Bertuol, D.A., 2017. Recovery of valuable materials from spent lithium ion batteries using electrostatic separation. International Journal of Mineral Processing 169, 91-98. 10.1016/j.minpro.2017.11.003
Standard, B., 2014. Determination of ceratin substances in electrochemical products, Part 5: Cadmium, lead and chromium in polymers and electronics cadmium and lead in metals by AAS, AFS, ICP-OES and ICP-MS. BSI Standard Publication.
Wang, X., Gaustad, G., Babbitt, C.W., 2016. Targeting high value metals in lithium-ion battery recycling via shredding and size-based separation. Waste Manag 51, 204-213. 10.1016/j.wasman.2015.10.026
Widijatmoko, S.D., Gu, F., Wang, Z., Hall, P., 2020. Selective liberation in dry milled spent lithium-ion batteries. Sustainable Materials and Technologies 23, e00134.
Winslow, K.M., Laux, S.J., Townsend, T.G., 2018. A review on the growing concern and potential management strategies of waste lithium-ion batteries. Resources, Conservation and Recycling 129, 263-277. 10.1016/j.resconrec.2017.11.001
Yu, M., Zhang, Z., Xue, F., Yang, B., Guo, G., Qiu, J., 2019. A more simple and efficient process for recovery of cobalt and lithium from spent lithium-ion batteries with citric acid. Separation and Purification Technology 215, 398-402. 10.1016/j.seppur.2019.01.027
Zeng, X., Li, J., Singh, N., 2014. Recycling of Spent Lithium-Ion Battery: A Critical Review. Critical Reviews in Environmental Science and Technology 44(10), 1129-1165. 10.1080/10643389.2013.763578
Zhang, T., He, Y., Ge, L., Fu, R., Zhang, X., Huang, Y., 2013. Characteristics of wet and dry crushing methods in the recycling process of spent lithium-ion batteries. Journal of Power Sources 240, 766-771. DOI:10.1016/j.jpowsour.2013.05.009
Zubi, G., Dufo-López, R., Carvalho, M., Pasaoglu, G., 2018. The lithium-ion battery: State of the art and future perspectives. Renewable and Sustainable Energy Reviews 89, 292-308. 10.1016/j.rser.2018.03.002